

Parametric Study of Nonequilibrium Shock Interference Patterns over a Fuselage-and-Wing Conceptual Vehicle

Catarina Garbacz^{*}, Fábio Morgado[†] and Marco Fossati[‡]
Aerospace Centre, University of Strathclyde, Glasgow, G1 1XJ, United Kingdom

Walter T. Maier[§], Brian C. Munguía[¶] and Juan J. Alonso^{||}
Stanford University, Stanford, CA 94305, U.S.A.

Adrien Loseille^{**}
INRIA, 1 Rue Honore d'Estienne d'Orves, 91120 Palaiseau, France

Predicting shock/shock and shock/boundary-layer interactions in gas flows that surround high-speed vehicles is key in aerodynamic design. Under typical hypersonic conditions, these flow structures are influenced by complex nonequilibrium phenomena leading to high-temperature effects. In this work, the conceptual Bedford wing-body vehicle is studied to analyse flow patterns in shock/shock and shock/boundary-layer interactions with thermochemical nonequilibrium. A parametric CFD study is carried out for different hypersonic operating conditions, with respect to the freestream Mach number. Simulations are performed with the SU2-NEMO solver coupled to the Mutation++ library, that provides all the necessary thermodynamic, kinetic and transport properties of the mixture and chemical species. The AMG library is used for automatic anisotropic mesh adaptation. Numerical results show that increasing the freestream Mach number from 4 to 10 leads to changes in the shock layer, locations of shock impingement and regions of boundary layer separation. Despite these changes, the change in freestream Mach number has little impact on the overall shock interaction structures.

I. Nomenclature

A = Millikan and White coefficient

B = Millikan and White coefficient

C = Reaction rate constant, $\text{cm}^3 \text{mol}^{-1} \text{s}^{-1}$

c = Mass fraction

D = Diffusion coefficient, $\text{m}^2 \text{s}^{-1}$

e = Energy per unit mass, J kg^{-1}

g = Degeneracy

h = Enthalpy per unit mass, J kg^{-1}

^{*}PhD student, Department Mechanical and Aerospace Engineering, AIAA Member, ana.gomes@strath.ac.uk

[†]PhD student, Department Mechanical and Aerospace Engineering, AIAA Member, fabio.pereira-morgado@strath.ac.uk

[‡]Associate Professor, Department Mechanical and Aerospace Engineering, AIAA Member, marco.fossati@strath.ac.uk

[§]PhD Student, Department of Aeronautics and Astronautics, AIAA Member, wmaier@stanford.edu

[¶]PhD Student, Department of Aeronautics and Astronautics, AIAA Member, bmunguia@stanford.edu

^{||}Professor, Department of Aeronautics and Astronautics, AIAA Associate Fellow, jjalonso@stanford.edu

^{**}Junior Scientist, INRIA Gamma3 team, AIAA Member, adrien.loseille@inria.fr

\vec{J} = Mass diffusion flux, $\text{kg m}^{-3}\text{s}^{-1}$

k = Reaction rate, $\text{cm}^3 \text{mol}^{-1}\text{s}^{-1}$

M = Molar mass, kg mol^{-1}

N = Number density, cm^{-3}

n = Number of species

p = Pressure, Pa

q = Conduction heat flux, kg s^{-3}

R_u = Universal gas constant, $\text{J mol}^{-1} \text{K}^{-1}$

T = Temperature, K

\vec{u} = Velocity, m s^{-1}

X = Molar fraction

θ = Characteristic temperature, K

λ = Thermal conductivity coefficient, $\text{W m}^{-1}\text{K}^{-1}$

μ = Viscosity coefficient, N s m^{-2}

ν' = Forward reaction stoichiometry coefficient

ν'' = Backward reaction stoichiometry coefficient

ρ = Density, kg m^{-3}

σ = Collision-limiting cross section, cm^2

τ = Relaxation time, s

$\bar{\tau}$ = Viscous stress tensor, $\text{kg m}^{-1} \text{s}^{-2}$

$\dot{\omega}$ = Chemical source term, $\text{kg m}^{-3} \text{s}^{-1}$

$\dot{\Omega}$ = Vibrational energy source term, $\text{J m}^{-3} \text{s}^{-1}$

Subscripts

A = Activation

b = Backward

f = Forward

i = Electronic level

k = Thermal energy mode

r = Reaction

s = Species

v = Vibrational level

Superscripts

C = Convective

c = Chemistry

e = Electronic energy mode

MW = Millikan and White

P = Park

r = Rotational energy mode

t = Translational energy mode

V = Viscous

v = Vibrational energy mode

II. Introduction

UNDERSTANDING the impact of shock interference patterns is necessary to accurately predict the severe aerothermal loads experienced by the surface of high-speed vehicles, e.g., during atmospheric re-entry or sustained hypersonic flight. High-Mach vehicles operate in flow regimes potentially dominated by high-temperature effects with intense heating, thermal nonequilibrium and finite-rate chemical kinetics. Nonequilibrium effects significantly influence the structure of shock interaction mechanisms, and in turn the aerothermodynamic loads on the vehicle's surface. Impinging shocks originating at the interference between shock waves emanating from the fuselage nose, wing, inlet cowls and high-lift devices can lead to catastrophic flight failures if not correctly predicted [1]. While the ability to numerically predict thermal and chemical nonequilibrium effects on canonical test cases is necessary to verify the physical and

numerical modelling, these cases often overlook the complex phenomena experienced on real vehicles during flight. As such, this work presents a numerical study of the aerothermodynamic environment around a vehicle known as Bedford wing-body [2] for different Mach numbers, with a focus on the shock patterns established under thermochemical nonequilibrium.

Extensive fundamental research has been done on the characterization of hyper-velocity flow over double-wedge and double-cone configurations highlighting shock/surface, shock/shock and shock/boundary layer interactions. These canonical configurations are widely studied as they serve as an approximation to the geometry of control surfaces, cowl and fuselage/canopy area. Early work by Hu *et al.* [3] studied the oscillations induced by shock/shock interactions over the double-wedge under the conditions of an inviscid multiple species flow and temperature dependent thermodynamic properties. It was found that oscillations were accompanied by the transition of shock interaction configurations. Tchien *et al.* [4, 5] continued on this work, adding real gas effects with Park's two-temperature model and finite-rate chemistry. This work confirmed that nonequilibrium effects alter the structure of the shock, shrinking the shock-layer compared to perfect ideal gases. Li *et al.* [6, 7] focused on the transition between type IV-V shock patterns by introducing the nonequilibrium relaxation length. By extending the shock polar method using this new parameter, Li was able to predict regional pressures and critical angles. Recently, Garbacz *et al.* [8] extended this analysis to CO₂ flows. The canonical double-wedge configuration was simulated for different sets of freestream conditions, finding that the shock pattern changes completely for a flow of air but not for the case of a CO₂-dominated flow, likely due to the vibrational modes being excited at much lower temperatures for the latter. Adding viscosity to the picture, some work has been done on the blunted cone, double-cone and cone-flare configurations, investigating the effects of shock/boundary layer interaction as well as axisymmetry. Nompelis *et al.* [9, 10] simulated a laminar double-cone under thermochemical nonequilibrium. It was found that failure to model the slip wall accurately leads to over-predictions of the heat transfer due to sensitivity of the vibrational energy accommodation coefficient. Additionally, the simulation was sensitive to not only the grid resolution, but the numerical schemes employed as well. Later, Knight *et al.* [11] simulated both high- and low-enthalpy N₂ flows over a laminar double-cone. The high-enthalpy results were in good agreement with experiments, however, low-enthalpy simulations displayed non-steady behavior not present in experiments. It was found that reducing the Reynolds number eliminated this unsteady phenomena. Hao *et al.* [12] builds upon the high-enthalpy simulation work by comparing the Park and CVDV (Coupled Vibration-Dissociation-Vibration [13]) nonequilibrium models. The double-cone was found to be especially sensitive to the vibration-dissociation models at high-enthalpies, with the CVDV model resulting in better agreement with experimental data. In a validation study, Koryukov *et al.* [14] found that failing to properly resolve the boundary layer can lead to significant discrepancies in the location of peak pressure coefficient values.

While these canonical cases allow for model testing, verification and validation, they often do not translate well

to real world vehicle flights. Generally, most of the studies on vehicles refer to simple capsules or blunted cones. However, there are few complex bodies that have been studied. Papadopoulos *et al.* [15] studied the X-38 vehicle in an effort to validate grid generation methodologies. With the grid generation technique, Papadopoulos was able to achieve fairly accurate results compared to experimental data. Scalabrin *et al.* [16] focused on the simulation of reentry configurations while accounting for thermochemical nonequilibrium. The RAM-C, the Mars entry capsule in the HYPULSE Expansion Tube, and a blunted cone in the CALSPAN shock tunnel were all simulated and compared to experimental data. Results agreed fairly well for the RAM-C and Mars entry vehicles, but heating and electron density for the blunted cone were over-predicted. Later on, Scalabrin was able to match results from the Apollo and FIRE-II capsules using both air-5-species and air-11-species gas models[17]. Sun *et al.* [18] and Qu *et al.* [19] both studied the X-33 aircraft as validation for improved numerical schemes. In both cases, a perfect ideal gas model was employed and the numerical schemes demonstrated improvement over past verification cases. Emelyanov *et al.* [20] expanded on these past experiments by simulating the X-51 vehicle with both thermal and chemical equilibrium.

Despite all of these previous works, there is still much to understand regarding complex real geometries that trigger shock/shock and shock/boundary-layer interactions, particularly in the presence of thermochemical nonequilibrium effects. This manuscript deals with the full-body geometry of the Bedford body, with a focus on the shock interactions. Simulations of air-5-species nonequilibrium hypersonic flow over this body are conducted for different values of Mach number: 4, 6, 8 and 10. The first case, $M = 4$, serves as validation since experimental data on the aerodynamic coefficients is available for comparison. Under the conditions studied, ionization is assumed not to play a role. Moreover, mesh adaptation is employed in this work, to ensure that the complex flow features are captured in the most accurate and computationally efficient manner. The paper first presents the governing equations, with particular attention paid to the thermal nonequilibrium and finite-rate chemistry closure terms. The next section then focuses on the numerical and solver methodology. Simulation results for the Bedford body are then shown and discussed. Finally, a summary of the main conclusions is presented.

III. Physical and numerical modeling

The system of governing equations is obtained following classical approaches presented in the literature for a laminar viscous, chemically-reacting, nonequilibrium flow [21]. The two-temperature model by Park [22] is used, where the translational energy mode is assumed to be at equilibrium with the rotational one, and the vibrational energy mode is assumed to be at equilibrium with the electronic one. In a compact form, the system can be described as

$$\frac{d\mathbf{U}}{dt} + \nabla \cdot \vec{\mathbf{F}}^C(\mathbf{U}) = \nabla \cdot \vec{\mathbf{F}}^V(\mathbf{U}) + \mathbf{Q}(\mathbf{U}), \quad (1)$$

where the conservative variables, convective fluxes, viscous fluxes and source terms are given, respectively, by

$$\mathbf{U} = \begin{pmatrix} \rho_1 \\ \vdots \\ \rho_{n_s} \\ \rho \vec{u} \\ \rho e \\ \rho e^{v-e} \end{pmatrix}, \quad \vec{\mathbf{F}}^C = \begin{pmatrix} \rho_1 \vec{u} \\ \vdots \\ \rho_{n_s} \vec{u} \\ \rho \vec{u} \otimes \vec{u} + p \vec{I} \\ \rho \vec{u} h \\ \rho \vec{u} e^{v-e} \end{pmatrix}, \quad \vec{\mathbf{F}}^V = \begin{pmatrix} \vec{J}_1 \\ \dots \\ \vec{J}_{n_s} \\ \vec{\tau} \\ \vec{\tau} \cdot \vec{u} + \sum_s \vec{J}_s h_s + \vec{q}^{v-e} + \vec{q}^{t-r} \\ \sum_s \vec{J}_s h_s^{v-e} + \vec{q}^{v-e} \end{pmatrix}, \quad \mathbf{Q} = \begin{pmatrix} \dot{\omega}_1 \\ \vdots \\ \dot{\omega}_{n_s} \\ 0 \\ 0 \\ \dot{\Omega} \end{pmatrix}, \quad (2)$$

and ρ is the density of the mixture, ρ_s is the partial density of the species, p is the static pressure, e and e^{v-e} are, respectively, the total energy per unit mass and the vibrational energy per unit mass for the mixture, h is the total enthalpy per unit mass, \vec{J}_s is the species mass diffusion flux, $\vec{\tau}$ is the viscous stress tensor, \vec{q} is the conduction heat flux, index s denotes the s^{th} chemical species and n_s is the total number of species.

Calculating the nonequilibrium thermodynamic state and source terms is necessary to close the system of governing equations that describes hypersonic flows. This is achieved by means of coupling with appropriate multi-temperature thermochemistry models. The equations presented below describe the implementation of the Park's two-temperature model [22] for a mixture composed of neutral species, provided by the Mutation++ library [23]. Each individual species is assumed to behave as an ideal gas. Hence, the total pressure of the mixture, p , is defined by Dalton's Law as the summation of the partial pressures associated with each species, p_s , determined by the ideal gas law,

$$p = \sum_{s=1}^{n_s} p_s = \sum_{s=1}^{n_s} \rho_s \frac{R_u}{M_s} T_{\text{tr}}, \quad (3)$$

where R_u is the universal gas constant, M_s is the molar mass of the species and T_{tr} is the trans-rotational temperature. The total specific energy of the flow e is given as the sum of the internal and kinetic energies:

$$e = \sum_{s=1}^{n_s} c_s e_s + \frac{1}{2} u^2, \quad (4)$$

where c_s is the mass fraction of the species, u is the magnitude of the flow velocity vector and e_s is the specific internal energy of the species, given by the sum of the energy of formation and the contribution of each internal mode,

$$e_s = e_s^i(T_{\text{tr}}) + e_s^r(T_{\text{tr}}) + e_s^v(T_{\text{ve}}) + e_s^e(T_{\text{ve}}) + e_s^0. \quad (5)$$

Using a combination of statistical thermodynamics and quantum mechanics, the internal mode energies are defined on

the basis of the Rigid-Rotor Harmonic Oscillator model (RRHO) as:

$$e_s^t(T_{tr}) = \frac{3}{2} \frac{R_u}{M_s} T_{tr}, \quad (6)$$

$$e_s^r(T_{tr}) = \begin{cases} \frac{R_u}{M_s} T_{tr}, & \text{for linear molecules,} \\ 0, & \text{for atoms,} \end{cases} \quad (7)$$

$$e_s^v(T_{ve}) = \begin{cases} \frac{R_u}{M_s} \sum_v \frac{\theta_{v,s}^v}{\exp(\theta_{v,s}^v/T_{ve}) - 1}, & \text{for molecules,} \\ 0, & \text{for atoms,} \end{cases} \quad (8)$$

$$e_s^e(T_{ve}) = \frac{R_u}{M_s} \frac{\sum_i g_{i,s} \theta_{i,s}^e \exp(-\theta_{i,s}^e/T_{ve})}{\sum_i g_{i,s} \exp(-\theta_{i,s}^e/T_{ve})}, \quad (9)$$

where $\theta_{v,s}^v$ is the characteristic vibrational temperature of the species and vibrational mode v , $g_{i,s}$ and $\theta_{i,s}^e$ are the degeneracy and characteristic electronic temperature, respectively, at energy level i for species s . The formation energy e_s^0 is referenced at the standard state conditions of 298.15 K and 1 atm.

The conservation equation for the mass of the mixture is replaced by a mass conservation equation for each species in the gas, incorporating a production/destruction term that results from chemical activity. The chemical source term $\dot{\omega}_s$ is given by

$$\dot{\omega}_s = M_s \sum_{r=1}^{n_r} (\nu''_{s,r} - \nu'_{s,r}) \left[k_{f,r} \prod_{j=1}^{n_s} \hat{\rho}_j^{\nu'_{j,r}} - k_{b,r} \prod_{j=1}^{n_s} \hat{\rho}_j^{\nu''_{j,r}} \right], \quad (10)$$

where n_r and n_s are respectively the number of reactions and the number of species, M_s is the molecular weight of the species, ν'_s is the forward reaction stoichiometry coefficient, ν''_s is the backward reaction stoichiometry coefficient, $\hat{\rho}$ is the molar density, $k_{f,r}$ is the forward reaction rate and $k_{b,r}$ is the backward reaction rate. The forward reaction rate for each reaction r is defined according to the modified Arrhenius equation [24]

$$k_{f,r} = C_r T^{-n} \exp\left(-\frac{T_A}{T_c}\right), \quad (11)$$

where the coefficients C_r , T_A and n are obtained from experimental data and are, respectively, the reaction rate constant, the activation temperature and an exponent. The backward reaction rates $k_{b,r}$ are determined from the equilibrium reaction rates, $k_{b,r} = k_{f,r}/k_{eq,r}$ for every reaction r . T_c is the controlling temperature determined by Park's two-temperature model [22]:

- Dissociation reactions $AB + M \rightleftharpoons A + B + M$

$$T_c = \sqrt{T_{tr}T_{ve}} \text{ for the forward rate; } T_c = T_{tr} \text{ for the backward rate;}$$

- Exchange reactions $AB + C \rightleftharpoons A + BC$

$$T_c = T_{tr}.$$

In the two-temperature model, the energy transfer mechanisms that determine the change in vibrational energy of the mixture, are accounted for in the source term vector. The source term, $\dot{\Omega}$, is defined as the sum of the vibrational-to-translational energy transfer and energy exchanges due to chemical activity,

$$\dot{\Omega} = \sum_{s=1}^{n_s} \dot{\Omega}_s^{t-r:v-e} + \dot{\Omega}_s^{c:v-e}. \quad (12)$$

The term $\dot{\Omega}_s^{t-r:v-e}$ concerns the rate of energy exchange between the translational and vibrational energy modes, following the Landau-Teller model [25],

$$\dot{\Omega}_s^{t-r:v-e} = \rho_s \frac{e_s^v(T) - e_s^v(T_v)}{\tau_s^{V-T}}. \quad (13)$$

The vibrational relaxation time of each species, τ_s^{V-T} , is given by the Millikan and White empirical formula [26] and the Park correction [27],

$$\tau_s^{V-T} = \tau_s^{MW} + \tau_s^P, \quad (14)$$

where the Millikan and White relaxation time of species depends on the vibrational relaxation times of the interactions with collision partners r , and the corresponding molar fractions, X_r , as follows

$$\tau_s^{MW} = \left(\sum_{r=1}^{n_s} \frac{X_r}{\tau_{s-r}^{MW}} \right)^{-1}, \quad (15)$$

$$\tau_{s-r}^{MW} = \exp \left(A_{s,r} \left(T^{-\frac{1}{3}} - B_{s,r} \right) - 18.42 \right) \left(\frac{P}{101325} \right)^{-1} [s]. \quad (16)$$

The Park correction is given by

$$\tau_s^P = \left(N_s \sigma_s \sqrt{\frac{8R_u T_{tr}}{\pi M_s}} \right)^{-1}, \quad (17)$$

where r denotes the r^{th} species, X_r is the molar fraction, N_s is the number density and σ_s is an effective cross-section for vibrational relaxation. It is assumed that molecules are destroyed or created at the average vibrational energy. Therefore

the change in vibrational-electronic energy of the mixture due to the production/destruction of species follows a simple non-preferential model and is accounted for in the term $\dot{\Omega}_s^{c:v-e}$, given by

$$\dot{\Omega}_s^{c:v-e} = \dot{\omega}_s e_s^{v-e}. \quad (18)$$

With regard to dissipative fluxes, the mass diffusion flux of each species \vec{J}_s is described by Fick's Law of diffusion:

$$\vec{J}_s = \rho D_s \vec{\nabla}(c_s) \quad (19)$$

where c_s is the species mass fraction and D_s is the species multicomponent diffusion coefficient, obtained by solving the Stefan-Maxwell equations under the Ramshaw approximation [28]. The viscous stress tensor is written in vector notation as:

$$\vec{\tau} = \mu \left(\nabla \vec{u} + \nabla \vec{u}^T - \frac{2}{3} \bar{I} (\nabla \cdot \vec{u}) \right) \quad (20)$$

where μ is the mixture viscosity coefficient. The conduction heat flux for each thermal energy mode, \vec{q}_k , is assumed to be given by Fourier's Law of heat conduction:

$$\vec{q}_k = \lambda_k \vec{\nabla}(T_k) \quad (21)$$

where T_k is the temperature and λ_k is the thermal conductivity coefficient of the k th energy mode. The mixture viscosity, μ , and thermal conductivity, λ_k , coefficients are determined by Wilke's mixing rule [29], with pure species properties determined from accurate collision integral data.

IV. SU2-NEMO solver, Mutation++ library and AMG mesh adaptation library

The open-source SU2 software suite* [30], written in C++ and Python, is the basis for this study. It is built specifically for the analysis of partial differential equations (PDEs) and PDE-constrained optimization problems on unstructured meshes with state-of-the-art numerical methods. The solver is rapidly establishing itself within the open-source community as a prominent software for multiphysics analysis and design, including the simulation of chemically-reactive and nonequilibrium flows [31] with the development of SU2-NEMO (NonEquilibrium MOdels solver). Extensive validation of the software is reported in the literature [30]. The-closure-of the governing equations for the system of interest is achieved by means of coupling with appropriate thermochemistry models (presented in section III). In this regard, the implementation in the present work extended SU2-NEMO by linking to the Mutation++ library† [23] (Multicomponent

*<https://github.com/su2code/SU2>

†<https://github.com/mutationpp/Mutationpp>

Thermodynamic And Transport properties for IONized gases in C++), that provides efficient algorithms for the computation of thermodynamic, transport (viscosity, thermal conductivity and diffusion) and chemical kinetic gas properties. The library has been designed for robustness over a wide range of temperatures and its accuracy in dealing with multi-temperature models, with the following constraints in mind: 1) high fidelity of the physical models, ensuring that the laws of thermodynamics are satisfied and that results are validated against existing experimental data, 2) low computational cost, 3) a modern, object-oriented, extensible framework, and 4) detailed in-source and user’s guide documentation in order to facilitate model improvement and collaboration. The library has been extensively validated as a software on its own [23] and some validation work has been carried out for the coupling of Mutation++ with the SU2-NEMO solver [32].

The pyAMG library developed by INRIA [‡] [33–36] is used in this work. PyAMG is a fast, robust and automatic tool that performs anisotropic mesh adaptation for complex geometries generating multi-scale and multi-direction phenomena in the flowfield (shock waves, contact discontinuities, boundary layers, turbulence, etc.). Given an initial mesh and associated CFD solution, a metric field is computed from interpolation error and surface geometric approximation. The metric field provides information about the desired element sizes and orientations in order to drive adaptation. For a finite volume solution, the interpolation error of any particular flow variable is second-order in space and can be approximated by the Hessian $\mathcal{H}(\mathbf{x})$. The Hessian is computed by pyAMG using a double \mathbf{L}^2 -projection [37]. The absolute value of the Hessian is used to ensure that the metric field is positive definite, and is given by

$$|\mathcal{H}| = \mathcal{R} |\Lambda| \mathcal{R}^T.$$

The optimal metric used in the adaptation procedure is given by the \mathbf{L}^p -norm normalization of the Hessian for a desired mesh complexity \mathcal{N} :

$$\mathcal{M}(\mathbf{x}) = \mathcal{N}^{\frac{2}{3}} \left(\int_{\Omega} (\det |\mathcal{H}(\mathbf{x})|)^{\frac{p}{2p+3}} d\Omega \right)^{-\frac{2}{3}} (\det |\mathcal{H}(\mathbf{x})|)^{-\frac{1}{2p+3}} |\mathcal{H}(\mathbf{x})| \quad (22)$$

where the constraint mesh complexity \mathcal{N} controls the desired number of DOFs in the output mesh, $\left(\int_{\Omega} (\det |\mathcal{H}(\mathbf{x})|)^{\frac{p}{2p+3}} d\Omega \right)^{-\frac{2}{3}}$ is a global normalization used to reach the desired number of DOFs, and $(\det |\mathcal{H}(\mathbf{x})|)^{-\frac{1}{2p+3}}$ is a local normalization which gives the sensitivity to small solution variations, and is dependent on the choice of norm. For example, the \mathbf{L}^1 -norm can be used to better capture small amplitude variations and has been shown to be effective for supersonic applications [38]. PyAMG performs successive local mesh modifications such as edge collapse, point insertion, edge swapping and point smoothing until the output mesh meets the metric requirements, as well as some mesh quality constraints to ensure the stability and enhance the performance of the CFD solver. The solution is then interpolated onto

[‡]<https://pyamg.saclay.inria.fr/>

the new mesh. More information about the process as well as detailed mathematical formulation can be found in [36].

V. Numerical test cases

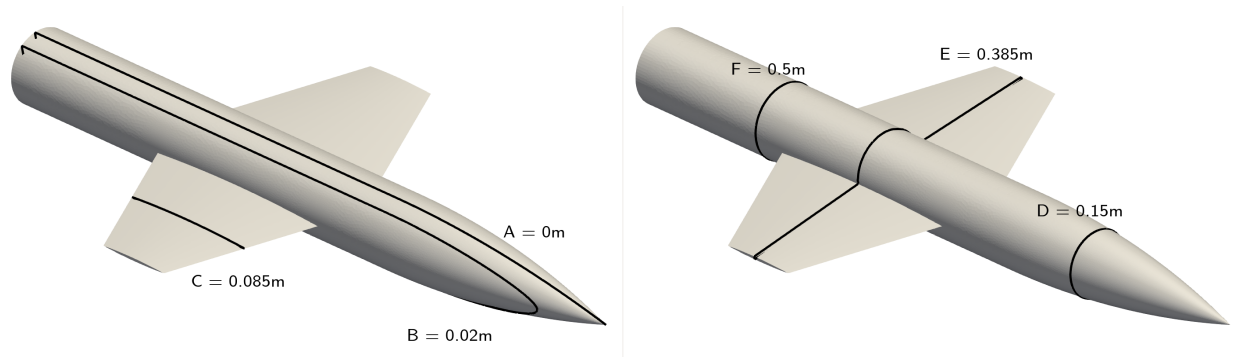


Fig. 1. Bedford wing-body: Section planes for visualisation along X and Y planes.

Results of the numerical study are presented in this section. The winged configuration studied in this work, known as Bedford wing-body, with symmetric lenticular wing section, is illustrated in Figure 1. Table 1 reports the conditions for which the simulations were performed. The choice of these conditions is based on the existence of validation data for the Bedford at Mach 4 (Bdf01). The Bedford cases at Mach 6, 8 and 10 (Bdf02 to Bdf04) have been considered as an investigation test case for which no reference data is available in the literature yet. For all test-cases, the standard air 5-species model is considered [39, 40].

Table 1. Parameters for the simulations

	Mach	α [deg]	T [K]	Reynolds	Y_{N_2}	Y_{O_2}	Y_{NO}	Y_N	Y_O
Bdf01	4	20	300	91,786	0.77	0.23	0.0	0.0	0.0
Bdf02	6	20	300	91,786	0.77	0.23	0.0	0.0	0.0
Bdf03	8	20	300	91,786	0.77	0.23	0.0	0.0	0.0
Bdf04	10	20	300	91,786	0.77	0.23	0.0	0.0	0.0

A. Grid adaptation

It is known that hypersonic flows typically generate high-gradient regions and highly-directional flow features such as shock waves, contact discontinuities, boundary layers, etc. When dealing with complex geometries, all these features are encountered in the flowfield as well as interactions between them. In this work, hybrid meshes are used, with a quasi-structured region consisting of prismatic elements capturing the boundary layer and the remaining part of the domain discretized in an unstructured manner with tetrahedral elements. To efficiently capture shock interference

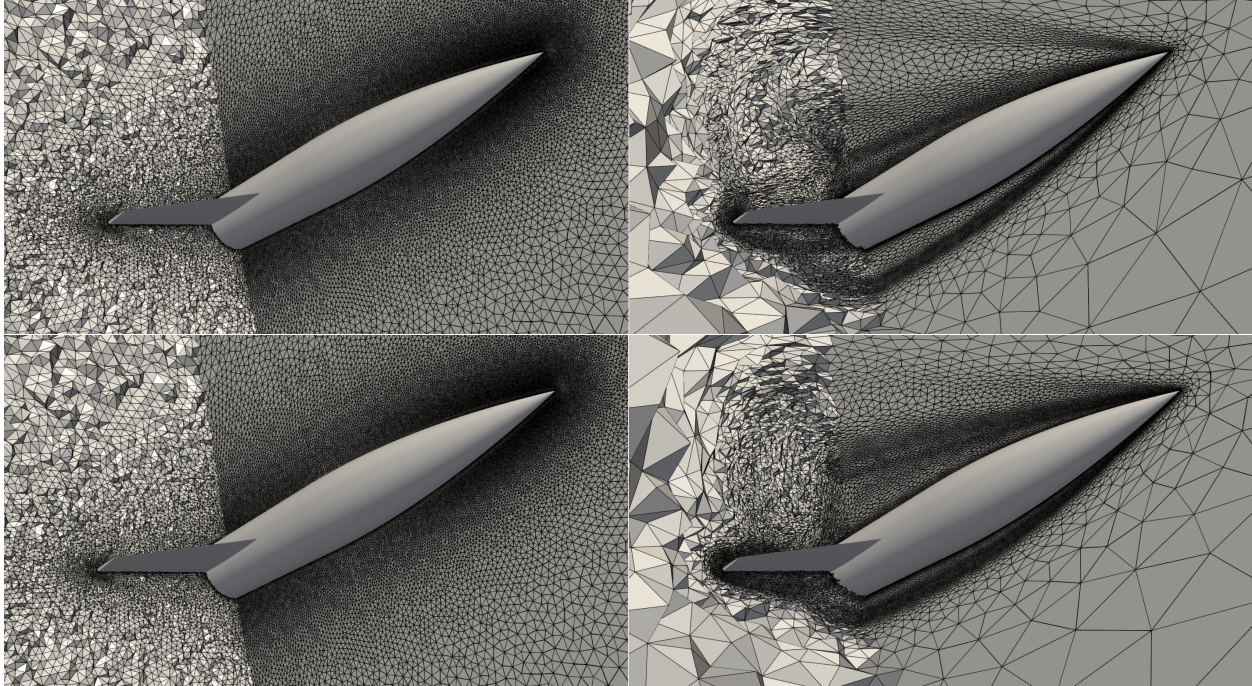


Fig. 2. Original and adapted meshes. Bedford wing-body at Mach 4 (top) and Mach 10 (bottom).

patterns in an accurate, yet computationally affordable way, automatic anisotropic mesh adaptation is used for the unstructured region, since it allows for flexibility to control the discretization both in element size, orientation and stretching. Controlling these grid parameters results in clustering of elements and alignment of cell interfaces with the flow features in such a way that no significant increase in number of nodes in the mesh is needed. In this work, the Mach number was chosen as a variable to compute the metric field used for adaptation. This choice was based on the fact that all relevant flow features (shocks, expansions, contact discontinuities, boundary layer, separations, vortices) translate to Mach number gradient, therefore guaranteeing that all of them will be captured in the adaptation process.

Table 2. Grid points and elements for adapted hybrid meshes.

	Number of points	Number of elements
Bdf01	2,111,391	10,699,929
Bdf02	2,048,479	10,325,863
Bdf03	2,026,373	10,196,352
Bdf04	2,087,754	12,275,162

The original viscous hybrid mesh is the same for all test-cases, with 11,473,410 elements and 3,109,217 grid points. After obtaining a first converged solution for each test-case, grid adaptation parameters are provided with two goals in mind: 1) keeping the number of nodes as close as possible to the initial mesh; 2) clustering and stretching grid elements

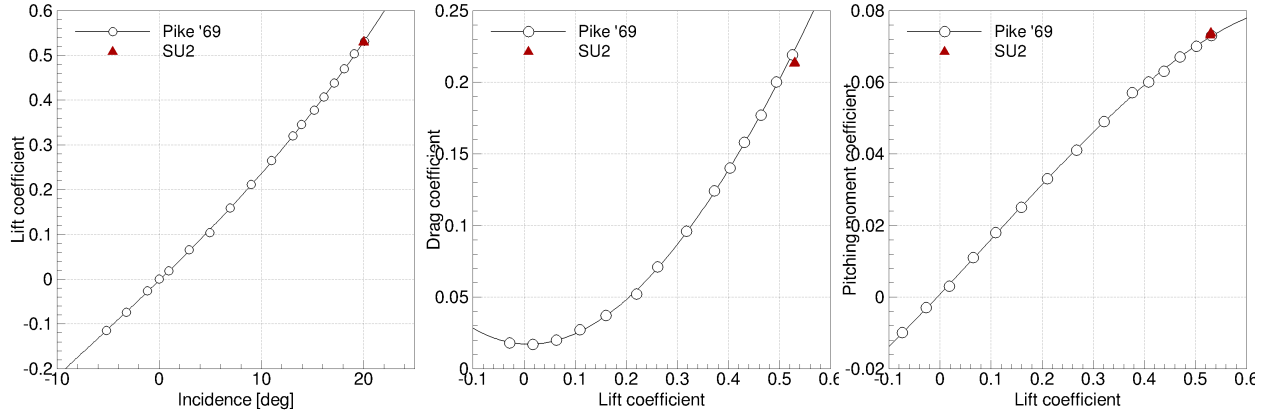


Fig. 3. Bedford wing-body at Mach 4: Comparison of aerodynamic coefficients with wind tunnel data.

in order to accurately capture sharp gradient regions, while keeping the mesh very coarse in regions of uniform flow or low-gradient. The first solution is then interpolated onto the resulting adapted grid and a new CFD simulation is performed. The process is repeated until grid independence is achieved. The number of grid points and elements for the final adapted hybrid mesh associated to each test-case is presented in Table 2. It is worth noticing that despite the slight reduction in number of grid points and elements (except for Bdf04 in the case of number of elements), improvement in accuracy has been obtained by the clustering of points in the relevant regions of the domain. In this analysis, more focus has been given to the shock wave structures below the body and near the wings where more interesting shock interference features are observed. This is seen in Figure 2, that shows the original mesh and the mesh at the end of the adaptation cycle for the lower and higher Mach cases, Bdf01 and Bdf04. As expected, the shock wave structure that envelopes the vehicle is closer to the body for the highest freestream Mach number. Figure 3 reports a comparison of the aerodynamic coefficients for the case of the Mach 4 flow with available experimental data. A good agreement is obtained for the final grid, thus validating the numerical results.

B. Parametric study

In this section, numerical results of the CFD simulation will be discussed for the planes A, B, C (parallel to fuselage axis) and D, E, F (along the wing spanwise direction) indicated in Figure 1. Planes A and B are slicing the fuselage longitudinally, while plane C is roughly at 50% of wing span. Planes D, E and F are respectively frontal slices before the wing, at 50% of fuselage corresponding to 50% of the wing chord and after the wing. To better understand the discussion that follows, an annotated flowfield is shown in Figure 4, where a schematic of the flow features that are encountered in the flow surrounding the Bedford vehicle is presented. For the angle of attack simulated in this work ($\alpha = 20^\circ$), the main flow features are the shock wave generated at the nose tip (stronger in the lower part of the vehicle), the shock wave that is generated at the leading edge (LE) towards the lower part of the wing and the interaction between the two. Furthermore, several expansion regions can be found: downstream of the nose shock, at the upper part of

the wing and at the tip of the wing. Boundary layer (BL) separation occurs at different locations resulting from shock impingement (wing and fuselage), flow incidence on the fuselage, wing-body junction, wing trailing edge (TE) typical separation and wake in the rear part of the vehicle. All of these generic features will be seen in the numerical results for each one of the test-cases in different shapes, locations and intensities.

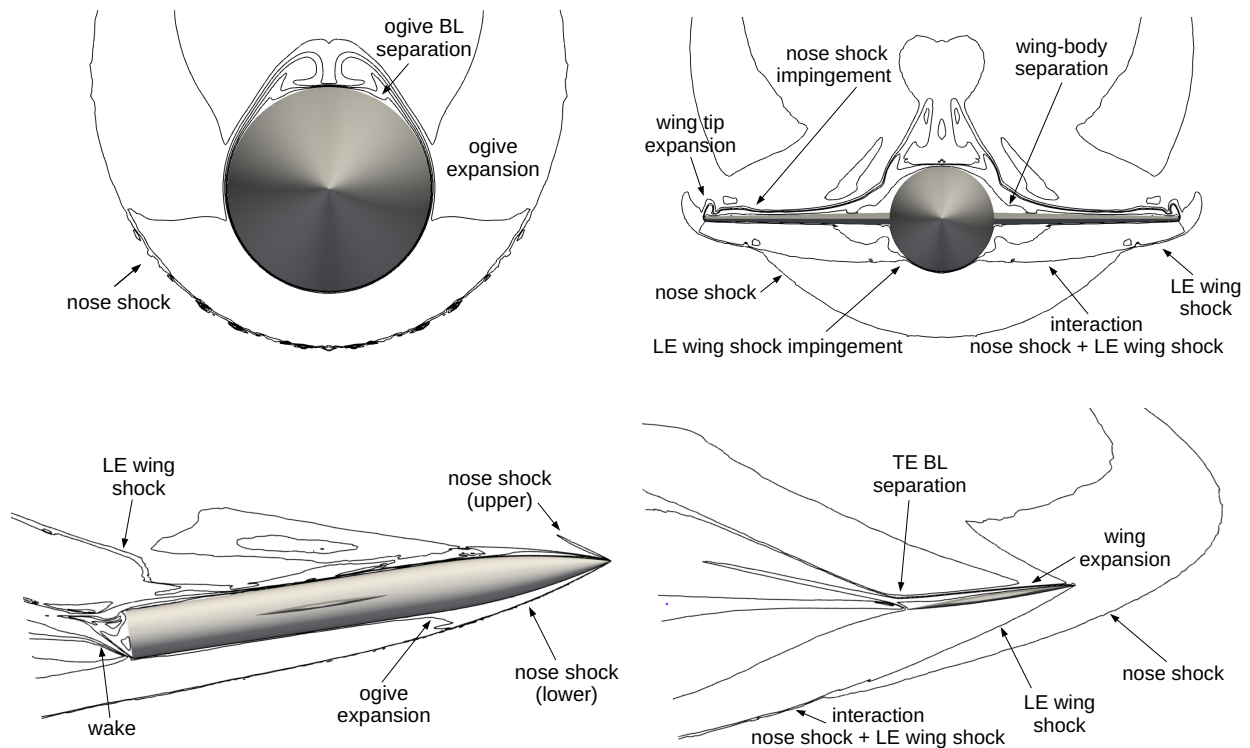


Fig. 4. Schematic of features encountered in the flowfield surrounding the Bedford vehicle.

Figure 5 report the obtained results for Mach number, for test-case Bdf01. Subplot 4a shows the plane of symmetry and subplots 5b and 5c show two other planes parallel to the plane of symmetry. Subplots 5d, 5e and 5f show planes normal to the fuselage axis. The strong attached shock wave generated by the nose tip towards the lower part of the vehicle is evident in the abrupt decrease in Mach number, as seen in subplot 5a. As expected from the value of the angle of attack, the upper shock wave is much weaker, with the corresponding contour lines in fading away not far from the body. As would be expected from the curved surface of the ogive, downstream of the initial deceleration caused from the nose tip, the change in geometry leads the flow to significantly expand after each one of the shock waves, which is indicated by the gradual increase in Mach number. This expansion is stronger in the lower part of the vehicle and is also evident in subplot 5d from a different perspective. Subplots 5b and 5d show that, due to the angle of attack and, consequently, the different incidence directions of the freestream flow on the upper and lower parts of the fuselage, the boundary layer thickens up to separation at a certain radial position in the fuselage. Further downstream, another strong

shock wave is generated by the leading edge of the wing towards the lower surface. It can be seen in subplot 5c and 5e that this shock wave interacts directly with the one generated in the nose tip. Subplot 5e shows the leading edge shock wave impinging on the fuselage surface, thus introducing an adverse pressure gradient and causing the boundary layer to separate. On the upper part of the wing, the flow undergoes a strong expansion, in which the flow significantly accelerates.

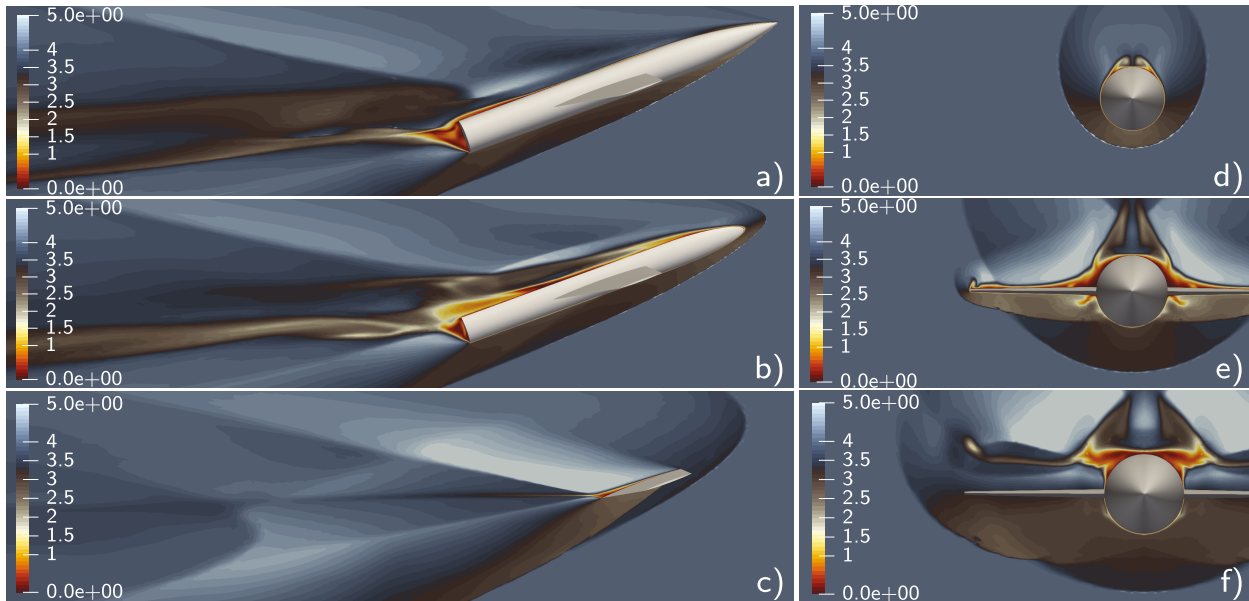


Fig. 5. Bedford wing-body Mach number contours at 20deg incidence and Mach 4. Y-axis sections (left), X-axis sections (right).

The development of a boundary layer on the surface of the wing causes the flow to compress up to the wall, just downstream of the leading edge - shown by the decrease in Mach number above the wing, in subplot 5e. The wing-body junction causes the flow to separate from the leading edge at the upper part of the wing (evident in subplot 5e). This separation together with the resulting compression wave can be visualized in subplots 5b and also further downstream in the plane of symmetry (subplot 5a), where in this case the boundary layer has reattached, likely due to the favourable pressure gradient arising from the fuselage-rear geometry change. Further away from the fuselage body, boundary layer separation on the upper surface of the wing only occurs closer to the trailing edge. Impingement of the nose shock on the upper surface of the wing is seen in in subplot 5e. Both the shock impingement and wing tip expansion introduce adverse pressure gradients in slightly different regions of the upper surface of the wing, causing the boundary layer to separate much before the trailing edge in that y-location - this can be observed in subplot 5e. The vortex generated in the wing-tip can be seen in both subplot 5e and 5f. Downstream of the wing, the boundary layer separation resulting from the different incidence directions of the flow (due to a non-zero angle of attack) also occurs. This is seen in subplots 5b and 5f. The adverse pressure gradient induced by the change in geometry in the rear part of the vehicle leads to flow separation in this region too. The wake of the flow can be seen in subplot 5a, where there is a clear region of very

low Mach number. With the weakening of flow disturbance, the flow then expands, and the Mach number gradually increases.

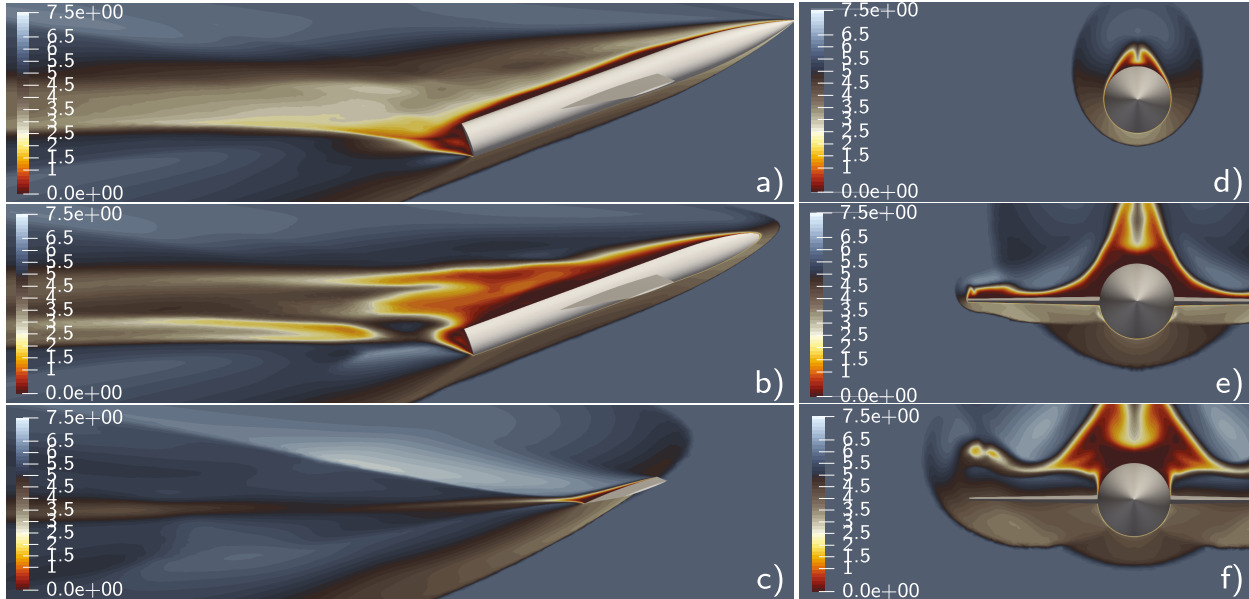


Fig. 6. Bedford wing-body Mach number contours at 20deg incidence and Mach 6. Y-axis sections (left), X-axis sections (right).

Figure 6 shows the Mach number contours for test-case Bdf02. As the freestream Mach number is increased from 4 to 6, some changes are observed in the flow patterns. Both upper and lower nose shocks are more attached to the fuselage body, which is seen in subplots 6a, 6d and 6e. The shock layer observed in the section shown in subplot 6e, below the fuselage, is smaller for Bdf02. The boundary layer separation resulting from the different incidence directions of the freestream flow on the ogive occurs closer to the nose tip, which is evident in subplot 6. Downstream of the vehicle, the wake of the flow also appears to be larger than for Bdf01. Similarly, the boundary layer separation caused by the wing-body junction on the upper part of the vehicle is significantly more pronounced, as the region of Mach < 1 is much larger for Bdf02, for the same x-plane shown in subplots 6e. However, it is not sufficiently large to extend to the plane of symmetry, where the boundary layer seems to be attached to the body but is significantly thicker along the whole fuselage, all the way up to the rear part of the vehicle. The impact of this larger separation is further seen in the plane shown in subplot 6b, where the region of Mach < 1 is much larger than for Bdf01. Both the nose tip shock wave and the shock wave generated by the wing leading edge are more attached to the body for Bdf02 than for Bdf01. As a consequence, the intersection between these two shocks is slightly closer to the vehicle as well, which is seen in subplot 6e. The boundary layer separation on the lower part of the fuselage, seen in subplot 6e, is still present for Bdf02, even though this disturbance seems to be less significant. The impingement of the nose shock on the wing is closer to the fuselage. The boundary layer separation resulting from this impingement, together

with a larger wing-body separation and the wing tip expansion cause the flow to be almost completely separated in the section shown in subplot 6e, as opposed to what was observed in case Bfd01. As for the wing section shown in subplot 6c, separation is also occurring earlier on, roughly at mid-chord, whereas for Bfd01 this was only occurring closer to the trailing edge. The vortex generated in the wing tip is slightly larger in this for Bdf02. Despite the differences observed between these two test-cases, Bdf01 and Bdf02, the overall shock interference features do not change.

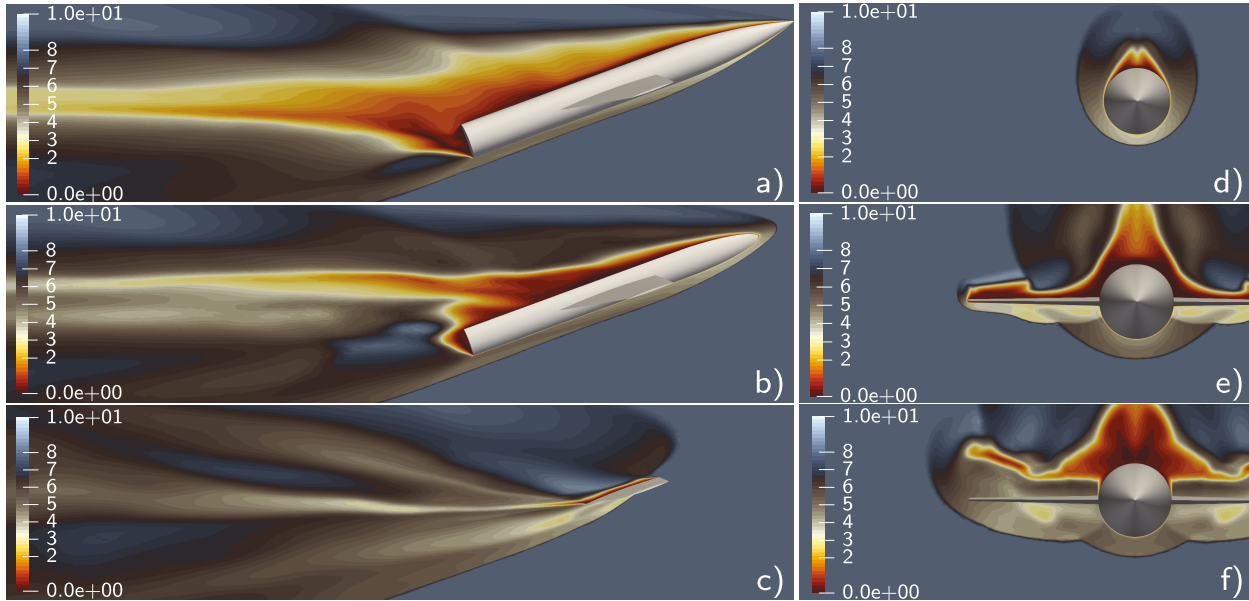


Fig. 7. Bedford wing-body Mach number contours at 20deg incidence and Mach 8. Y-axis sections (left), X-axis sections (right).

Figure 7 shows the Mach number contours for test-case Bdf03. Overall, the trend of the flow pattern observed between Bfd01 and Bfd02 extends to this test-case. The nose shock structure that envelops the body is closer to the vehicle, as seen in subplots 7a and 7d. The nose shock that develops towards the upper part of the flowfield is significantly stronger than for the two previous cases, where this trend was already visible. For what concerns the wing region, the increasing region of boundary layer separation with low Mach number on top of the fuselage is noticeable in subplot 7e. This region now extends up to the plane of symmetry, which is also seen in subplot 7a. As opposed to what is observed for Bdf01 and Bdf02, this causes the boundary layer to be separated downstream of the wing, up until the rear part of the vehicle. At the lower part of the fuselage, subplot 7e, the impingement of the leading edge shock wave seems to have less impact on the boundary layer, with a smaller separation region (not visible in the images). Looking at subplot 7c, the boundary layer thickens from the leading edge all the way along the chord, contrary to what was observed in Bdf01 and Bdf02. Another evident difference is the appearance of low Mach regions, denoted by a lighter yellow region in subplot 7f. It is inferred that this difference is likely due to the increasing impact of thermal nonequilibrium effects. This is supported by the fact that these are the regions where the significant vibrational

excitation occurs, which can be seen in subplot 7e of of Figure 10, that compares vibrational temperature for the different test-cases. The presence of nonequilibrium effects and its impact on the flowfield is discussed in more detail in the section.

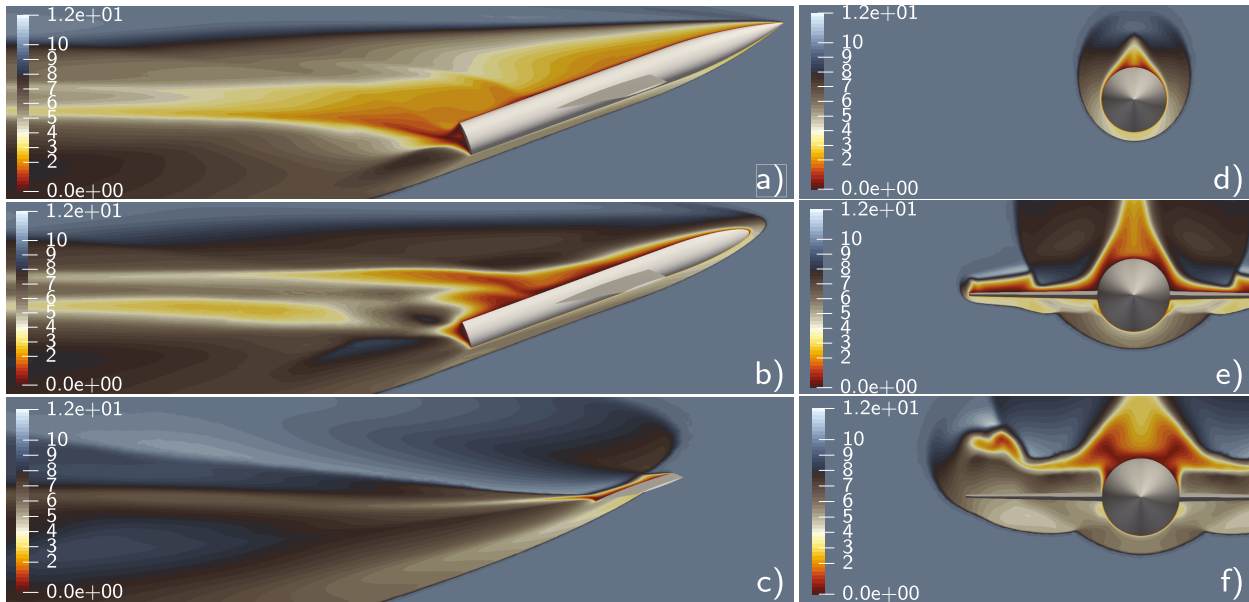


Fig. 8. Bedford wing-body Mach number contours at 20deg incidence and Mach 10. Y-axis sections (left), X-axis sections (right).

Figure 8 shows the Mach number contours for test-case Bdf04. With the further increase in freestream Mach number, the conical shock from the ogive nose gets closer to the vehicle. The trend of having a stronger upper nose shock is maintained with the increase of Mach number, being Bdf04 the case where this shock wave seems to be stronger with contours that are more defined (subplot 8a). On the contrary, the trend that has been observed for the behaviour of the boundary layer in the upper part of the fuselage (plane of symmetry, subplot 8a) does not extend to this test-case. For Bdf04, the boundary layer in this region is thin up to the point of interaction with the wing leading edge shock. The impact of this shock is still evident in the plane of symmetry downstream of the wing. A thickening of the boundary layer and a small separation is observed in this region. Downstream of the shock, the boundary layer reattaches. Moreover, the boundary layer separation resulting from leading edge shock impingement on the lower part of the fuselage is more significant than for the previous test-case, which can be seen subplots 8e and 8f. In subplot 8c, the impingement of the nose shock on the upper part of the wing is evident, causing the boundary layer to separate. Reattachment follows, given the acceleration of the flow occurring in this region, associated to the expansion wave that is observed.

Despite some differences observed in the flowfield for different test-cases, overall, the shock wave pattern does not change. Table 3 reports the aerodynamic coefficients for this study. As expected in supersonic flight, both drag and lift coefficient, as well as the Lift/Drag ratio decrease with the increase of Mach number. The last column in Table 3 reports

Table 3. Aerodynamic coefficients and heat flux.

Mach	Lift Coefficient	Drag Coefficient	Lift/Drag	Peak heat flux along wing [W/m ²]
4	0.5371	0.23961	2.242	4.732 e+6
6	0.3935	0.20377	1.931	5.210 e+6
8	0.3719	0.19218	1.935	7.889 e+6
10	0.3494	0.19099	1.830	1.025 e+7

the peak heat flux on the wing of the vehicle typically occurring in the region where the conical shock from the ogive nose intersects the wing.

C. Nonequilibrium effects

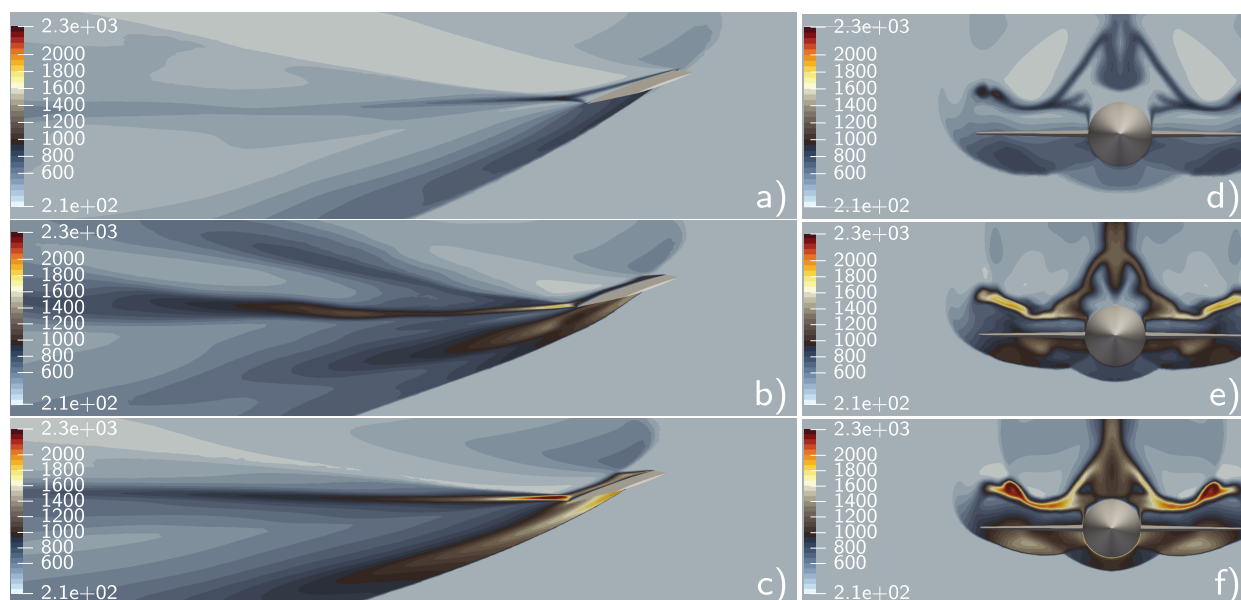


Fig. 9. Comparative view of Translational-Rotational Temperature contours. Y-axis sections at (left), X-axis sections (right). From top to bottom Mach 6, Mach 8 and Mach 10.

Figures 9 and 10 shows the contours of translational and vibrational temperature for the wing x- and y-planes, for all test-cases Bdf01 to Bdf04. The difference between translational and vibrational temperatures is a measure of the degree of thermal nonequilibrium occurring in the flowfield, and the values of vibrational temperature indicate the extent to which the vibrational energy modes of the molecules have been excited, due to the energy transferred from translational energy modes. Results are not shown for Bdf01 since the excitation of vibrational modes is negligible and values of vibrational temperature remain the same as the freestream for such a freestream Mach number. The trend observed as the Mach number increases is also predicted: regions with vibrational temperature higher than the freestream value are larger. The regions where vibrational excitation is expected to be more significant are regions behind shock waves,

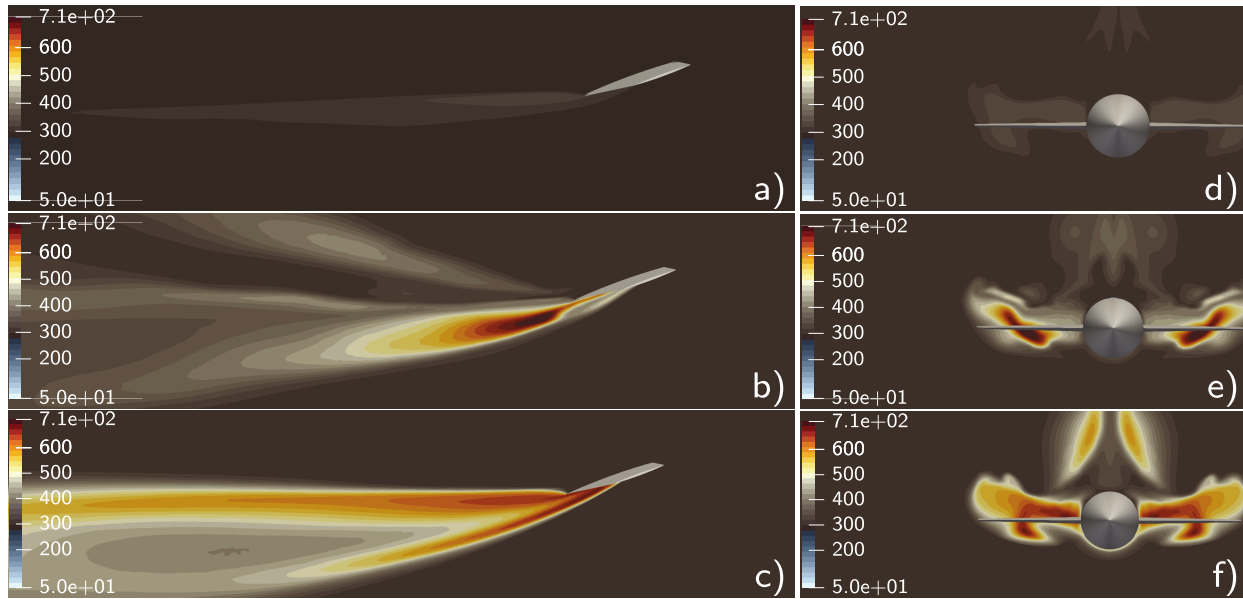


Fig. 10. Comparative view of Vibrational-Electronic Temperature contours. Y-axis sections at (left), X-axis sections (right). From top to bottom Mach 6, Mach 8 and Mach 10.

further downstream. Shock waves, or compression waves, increase the translational internal energy of the flow and, only after a certain time, this energy relaxes towards the excitation of vibrational degrees of freedom of molecules. Therefore, after a sudden increase in translational temperature, the larger the time scales of the flow (regions of low velocity), the stronger is the impact of this energy exchange mechanism. This is seen in the numerical results, as the regions where vibrational temperature contours are more relevant are, accordingly, post-shock or post-compression regions where the flow slows down. When it comes to thermal nonequilibrium, it is observed that the strongest discrepancies between translational vibrational temperature increase with Mach number.

For what concerns chemical nonequilibrium, results are only shown for Bdf04, since for the remaining test-cases, chemical activity is negligible or non-existent and the flow can be considered as frozen. Figure 11 shows mass fractions of species O_2 , N_2 , NO and O for Bdf04. The reasoning of relaxation time applies to finite-rate chemistry as well. An increase in the internal energy of the flow is necessary to trigger dissociation processes, that in turn have an associated incubation time before they become relevant. As such, numerical results are shown for the plane of symmetry, since the strongest chemical activity occurs in the wake of the flow, where Mach number is very low. Some changes in mass fractions can also be observed in the region of boundary layer separation on the upper part of the vehicle, especially when it comes to N_2 mass fractions. The change in mass fractions indicates that both N_2 and O_2 dissociation reactions are triggered, as well as exchange reactions that result in NO formation. For the plane of symmetry, there is significant amount of atomic oxygen, with a maximum value of 30%, which is expected due to the fact that O_2 dissociation is the first type of reaction to be activated [24].

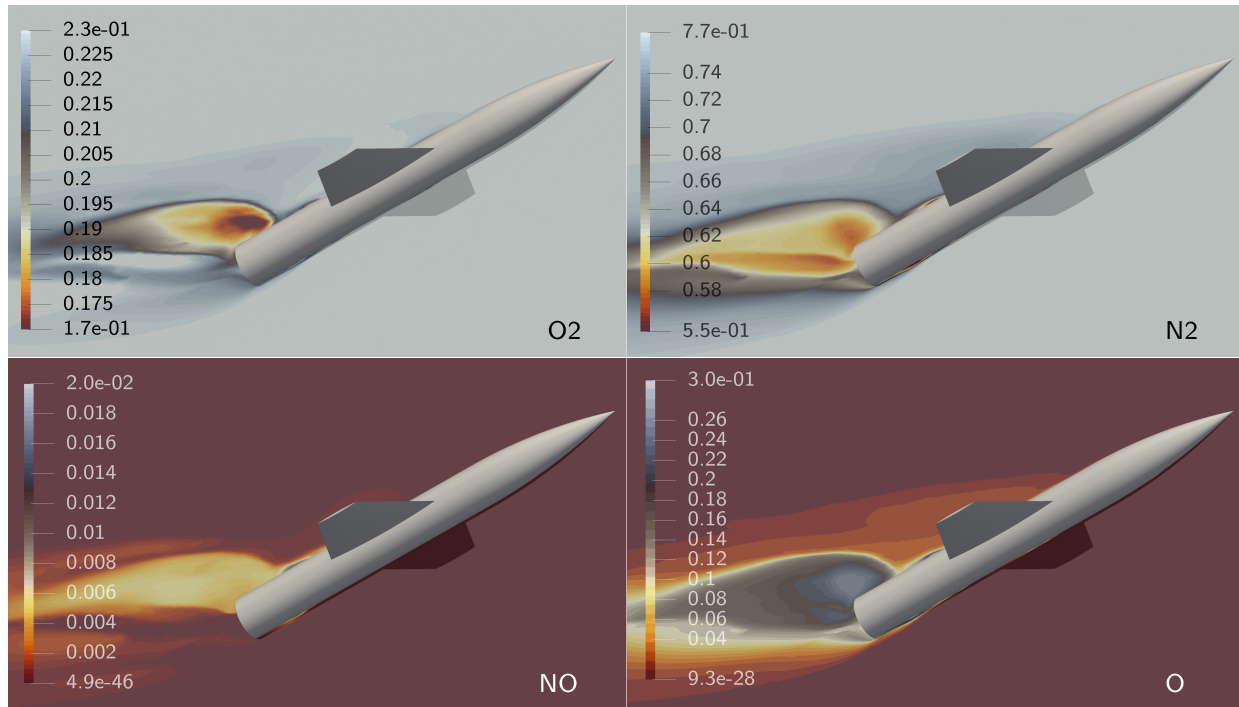


Fig. 11. Bedford wing-body at Mach 10: Mass fractions.

VI. Conclusions

A numerical study on the shock/shock and shock/boundary-layer interactions occurring in the flow field surrounding a winged high-speed vehicle is presented. High-temperature gas effects typically encountered in hypersonic flight conditions are taken into account. A parametric study of the nonequilibrium flow over the Bedford wing-body configuration is performed to understand how the interactions patterns change when the freestream Mach number is increased. Mach 4, 6, 8 and 10 flows are simulated. Results for the first test-case are validated against experimental data, and Mach 6 to 10 cases are considered as investigation test-cases. Automatic mesh adaptation is used to guarantee accurate predictions with no excessive computational cost and to ensure that the shock interference pattern are represented with grid independent predictions. The shock interference structures and the interactions with the boundary layer in the most critical regions are described. As the freestream Mach number increases, some differences in the flow features are observed, such as shock layer, locations of shock impingement as well as behaviour of the boundary layer and regions of separation. Chemical reactions are activated only for Mach 10 whereas vibrational excitation occurs from Mach 6 to 10, being more relevant as the Mach number increases. Overall, the shock interaction pattern does not change. The extension of this study to other hypersonic vehicle configurations and/or to the atmosphere of Mars is being considered.

Acknowledgments

The authors wish to acknowledge the support the EPSRC funded ARCHIE-WeSt High Performance Computer (www.archie-west.ac.uk). EPSRC grant no. EP/K000586/1. The authors would also like to thank for Brian Munguia for providing his expertise.

References

- [1] Watts, J. D., "Flight Experience with Shock Impingement and Interference Heating on the X-15-A Research Airplane," Technical Paper TM X-1669, NASA, Oct. 1968.
- [2] Pike, J., "Wind Tunnel Tests on Six Wing-Body Models at $M=4$," Tech. rep., Aeronautical Research Council. ARC/CP-1074, 1969.
- [3] Hu, Z. M., Myong, R. S., Wang, C., Cho, T. H., and Jiang, Z. L., "Numerical study of the oscillations induced by shock/shock interaction in hypersonic double-wedge flows," *Shock Waves*, Vol. 18, No. 1, 2008, p. 41. doi:10.1007/s00193-008-0138-x.
- [4] Tchien, G., Fogue, M., Burtshell, Y., Zeitoun, D., and Ben-Dor, G., "Shock-on-shock interactions over double-wedges: comparison between inviscid, viscous and nonequilibrium hypersonic flow," *Shock Waves*, edited by K. Hannemann and F. Seiler, Springer Berlin Heidelberg, Berlin, Heidelberg, 2009, pp. 1497–1502. doi:10.1007/978-3-540-85181-3_114.
- [5] Tchien, G., Burtshell, Y., and Zeitoun, D. E., "Numerical study of the interaction of type IVr around a double-wedge in hypersonic flow," *Computers Fluids*, Vol. 50, No. 1, 2011, pp. 147 – 154. doi:10.1016/j.compfluid.2011.07.002".
- [6] Li, J., Zhu, Y., and Luo, X., "On Type VI-V transition in hypersonic double-wedge flows with thermo-chemical non-equilibrium effects," *Physics of Fluids*, Vol. 26, No. 8, 2014, p. 086104. doi:10.1063/1.4892819.
- [7] Li, J., Zhu, Y., and Luo, X., "Thermochemical Non-equilibrium Effects on Type VI-V Transition in Hypersonic Double-Wedge Flow," *29th International Symposium on Shock Waves 1*, edited by R. Bonazza and D. Ranjan, Springer International Publishing, Cham, 2015, pp. 167–172. doi:10.1007/978-3-319-16835-7_24.
- [8] Garbacz, C., Fossati, M., Maier, W., Alonso, J. J., Scoggins, J., Magin, T., and Economon, T. D., "Numerical Study of Shock Interference Patterns for Gas Flows with Thermal Nonequilibrium and Finite-Rate Chemistry," *AIAA Scitech 2020 Forum*, 2020, p. 1805. doi:10.2514/6.2020-1805.
- [9] Nompelis, I., Candler, G. V., and Holden, M. S., "Effect of vibrational nonequilibrium on hypersonic double-cone experiments," *AIAA journal*, Vol. 41, No. 11, 2003, pp. 2162–2169. doi:10.2514/2.6834.
- [10] Nompelis, I., "Computational study of hypersonic double-cone experiments for code validation," Ph.D. thesis, University of Minnesota, 2004.
- [11] Knight, D., Longo, J., Drikakis, D., Gaitonde, D., Lani, A., Nompelis, I., Reimann, B., and Walpot, L., "Assessment of CFD capability for prediction of hypersonic shock interactions," *Progress in Aerospace Sciences*, Vol. 48, 2012, pp. 8–26. doi:10.1016/j.paerosci.2011.10.001.

- [12] Hao, J., Wang, J., and Lee, C., "Numerical simulation of high-enthalpy double-cone flows," *AIAA Journal*, 2017, pp. 2471–2475. doi:10.2514/1.J055746.
- [13] Marrone, P. V., and Treanor, C. E., "Chemical Relaxation with Preferential Dissociation from Excited Vibrational Levels," *The Physics of Fluids*, Vol. 6, No. 9, 1963, pp. 1215–1221. doi:10.1063/1.1706888.
- [14] Koryukov, I., and Kryukov, I., "Three-dimensional calculation of the aerothermodynamics of a double cone 25°/55° on an unstructured grid," *Journal of Physics: Conference Series*, Vol. 1009, IOP Publishing, 2018, p. 012003. doi:10.1088/1742-6596/1009/1/012003.
- [15] Papadopoulos, P., Venkatapathy, E., Prabhu, D., Loomis, M. P., and Olynick, D., "Current grid-generation strategies and future requirements in hypersonic vehicle design, analysis and testing," *Applied Mathematical Modelling*, Vol. 23, No. 9, 1999, pp. 705–735. doi:10.1016/S0307-904X(99)00007-4.
- [16] Scalabrin, L., and Boyd, I., "Numerical simulation of weakly ionized hypersonic flow for reentry configurations," *9th AIAA/ASME Joint Thermophysics and Heat Transfer Conference*, 2006, p. 3773. doi:10.2514/6.2006-3773.
- [17] Scalabrin, L. C., "Numerical simulation of weakly ionized hypersonic flow over reentry capsules," *Education*, Vol. 130, No. 4, 2007.
- [18] Sun, D., Qu, F., and Yan, C., "An effective flux scheme for hypersonic heating prediction of re-entry vehicles," *Computers & Fluids*, Vol. 176, 2018, pp. 109–116. doi:10.1016/j.compfluid.2018.05.028.
- [19] Qu, F., Sun, D., Zuo, G., and Shi, Y., "An improvement on the AUSMPWM scheme for hypersonic heating predictions," *International Journal of Heat and Mass Transfer*, Vol. 108, 2017, pp. 2492–2501. doi:10.1016/j.ijheatmasstransfer.2016.12.031.
- [20] Emelyanov, V., Karpenko, A., and Volkov, K., "Simulation of hypersonic flows with equilibrium chemical reactions on graphics processor units," *Acta Astronautica*, Vol. 163, 2019, pp. 259–271. doi:10.1016/j.actaastro.2019.01.010.
- [21] Gnoffo, P., Gupta, R., and Shinn, J., "Conservation equations and physical models for hypersonic air flows in thermal and chemical nonequilibrium," NASA Technical Paper 2867, 1989, p.158.
- [22] Park, C., "Assessment of two-temperature kinetic model for ionizing air," *Journal of Thermophysics and Heat Transfer*, Vol. 3, No. 3, 1989, pp. 233–244. doi:10.2514/3.28771.
- [23] Scoggins, J., and Magin, T., "Development of Mutation++: Multicomponent Thermodynamic and Transport Properties for Ionized Plasmas written in C++," 2014. doi:10.2514/6.2014-2966.
- [24] Anderson, J., *Hypersonic and High-temperature Gas Dynamics*, AIAA education series, American Institute of Aeronautics and Astronautics, 2006.
- [25] Landau, L., and Teller, E., *Physik Zeitschrift der Sowjetunion*, Vol. 10, 1936, pp. 34–38.

- [26] Millikan, R. C., and White, D. R., "Systematics of Vibrational Relaxation," *The Journal of Chemical Physics*, Vol. 39, No. 12, 1963, pp. 3209–3213. doi:10.1063/1.1734182.
- [27] Park, C., "Assessment of two-temperature kinetic model for ionizing air," *Journal of Thermophysics and Heat Transfer*, Vol. 3, No. 3, 1989, pp. 233–244. doi:10.2514/3.28771.
- [28] Scoggins, J. B., "Development of numerical methods and study of coupled flow, radiation, and ablation phenomena for atmospheric entry," Ph.D. thesis, von Karman Institute for Fluid Dynamics, 9 2017.
- [29] Wilke, C. R., "A Viscosity Equation for Gas Mixtures," *The Journal of Chemical Physics*, Vol. 18, No. 4, 1950, pp. 517–519. doi:10.1063/1.1747673.
- [30] Economon, T. D., Palacios, F., Copeland, S. R., Lukaczyk, T. W., and Alonso, J. J., "SU2: An Open-Source Suite for Multiphysics Simulation and Design," *AIAA Journal*, Vol. 54, No. 3, 2016, pp. 828–846. doi:10.2514/1.J053813.
- [31] Palacios, F., Copeland, S., Lonkar, A., and Alonso, J., "Adjoint-Based Goal-Oriented Mesh Adaptation for Nonequilibrium Hypersonic Flows," *51st AIAA Aerospace Sciences Meeting including the New Horizons Forum and Aerospace Exposition 2013*, AIAA Paper 2013-0552, 2013. doi:10.2514/6.2013-552.
- [32] Garbacz, C., Fossati, M., Maier, W., Alonso, J. J., Scoggins, J., Magin, T., and Economon, T. D., "Numerical Study of Shock Interference Patterns for Gas Flows with Thermal Nonequilibrium and Finite-Rate Chemistry," *AIAA Scitech 2020 Forum, Orlando, FL*, AIAA Paper 2020-1805 (2020). doi:10.2514/6.2020-1805.
- [33] Loseille, A., and Loehner, R., "Boundary Layer Mesh Generation and Adaptivity," 2011. doi:10.2514/6.2011-894.
- [34] Loseille, A., and Menier, V., "Serial and Parallel Mesh Modification Through a Unique Cavity-Based Primitive," *Proceedings of the 22nd International Meshing Roundtable*, edited by J. Sarrate and M. Staten, Springer International Publishing, Cham, 2014, pp. 541–558. doi:10.1007/978-3-319-02335-9_30.
- [35] Loseille, A., Menier, V., and Alauzet, F., "Parallel Generation of Large-size Adapted Meshes," *Procedia Engineering*, Vol. 124, 2015, pp. 57 – 69. doi:10.1016/j.proeng.2015.10.122, 24th International Meshing Roundtable.
- [36] Loseille, A., "Unstructured Mesh Generation and Adaptation," *Handbook of Numerical Methods for Hyperbolic Problems - Applied and Modern Issues*, edited by R. Abgrall and C.-W. Shu, Elsevier, 2017, pp. 263–302. doi:10.1016/bs.hna.2016.10.004.
- [37] Vallet, M.-G., Manole, C.-M., Dompierre, J., Dufour, S., and Guibault, F., "Numerical comparison of some Hessian recovery techniques," *International Journal for Numerical Methods in Engineering*, Vol. 72, No. 8, 2007, pp. 987–1007.
- [38] Frazza, L., "3D anisotropic mesh adaptation for Reynolds Averaged Navier-Stokes simulations." Ph.D. thesis, 2018.
- [39] Park, C., "Review of chemical-kinetic problems of future NASA missions. I - Earth entries," *Journal of Thermophysics and Heat Transfer*, Vol. 7, No. 3, 1993, pp. 385–398. doi:10.2514/3.431.
- [40] Park, C., Jaffe, R. L., and Partridge, H., "Chemical-Kinetic Parameters of Hyperbolic Earth Entry," *Journal of Thermophysics and Heat Transfer*, Vol. 15, No. 1, 2001, pp. 76–90. doi:10.2514/2.6582.